Article

Synthesis of BaZrS₃ Perovskite Thin Films at a Moderate Temperature on Conductive Substrates

Corrado Comparotto,* Petter Ström, Olivier Donzel-Gargand, Tomas Kubart, and Jonathan J. S. Scragg

Cite This: *ACS Appl. Energy Mater.* 2022, 5, 6335–6343

Read Online

ACCESS | 📊 Metrics & More | 📖 Article Recommendations | 🆂🆘 Supporting Information

ABSTRACT: Chalcogenide perovskites are being considered for various energy conversion applications, not least photovoltaics. BaZrS₃ stands out for its highly stable, earth-abundant, and nontoxic nature. It exhibits a very strong light–matter interaction and an ideal band gap for a top subcell in a two-junction photovoltaic device. So far, thin-film synthesis—necessary for proper optoelectronic characterization as well as device integration—remains underdeveloped. Sputtering has been considered, among others, but the need for an annealing step of at least 900 °C has been a cause for concern: such a high temperature could lead to damaging the bottom layers of prospective tandem devices. Still, a solid-state fabrication route has already demonstrated that BaZrS₃ can form at much lower temperatures if excess S is present. In this work, sputtered Ba–Zr precursors capped by SnS are sulfurized at under 600 °C for 20 min. Although some Sn is still present at the surface after sulfurization, the resulting crystalline quality is comparable to samples synthesized at much higher temperatures. The results are rationalized, and the effect of key process variables is examined. This study represents the first successful synthesis of BaZrS₃ perovskite that is compatible with conductive substrates—an important step forward for device integration.

KEYWORDS: chalcogenides, perovskites, sputtering, photovoltaics, thin films
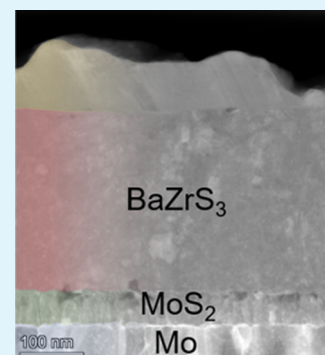
1. INTRODUCTION

Crystalline silicon (c-Si) has been dominating the photovoltaics (PV) market since its birth and is expected to remain the leading technology in the near future.[1,2] The theoretical maximum power conversion efficiency of a single-junction c-Si PV cell is around 29%,[3,4] and the state-of-the-art technology is approaching this point.[5] However, if a second p–n junction is stacked on top of the c-Si cell, the efficiency limit is increased to ca. 43%.[6] The advent of efficient lead halide perovskite absorbers with band gaps in the range of 1.6–1.8 eV has opened a new path toward inexpensive two-junction solar cells.[6] Such tandem devices have already demonstrated an efficiency of almost 30%,[7] but two main concerns need to be addressed to take this technology to mass production. The first one is the intrinsic chemical instability of lead halide perovskites, resulting in performance degradation during long-term operation.[8,9] The second concern is the presence of toxic Pb.[10] Alternative (nonhalide) perovskites that possess greater intrinsic chemical stability could circumvent both issues, although as yet, no such candidate has demonstrated comparable performance. To this end, chalcogenide perovskites have been increasingly considered.[11–16] In 2015, Sun et al. theoretically screened this class of compounds and proposed them for PV applications for the first time.[11] Since then, chalcogenide perovskites have already experimentally demonstrated outstanding chemical and optoelectronic properties. Their absorption coefficient is greater than 10^5 cm^{-1} near the band edge, the highest among all known solar cell

materials.[12,17] Niu et al. and Xu et al. demonstrated their remarkable stability, showing that they can withstand heating in air up to at least 400 °C.[14,18] Although many ABX₃ chalcogenide compounds have been proposed theoretically, only a few achieve a stable ground state with the perovskite structure, and all of them are sulfides. BaZrS₃ and BaHfS₃ are two examples, while a few more including SrZrS₃ can be grown under certain conditions.[19] This explains why the majority of the experimental work to date concerns BaZrS₃. Gupta et al. proved the superior stability of BaZrS₃ over the typical halide perovskite MAPbI₃ by directly comparing the responsivity of perovskite-based photodetectors during ambient storage and steam exposure.[20] They attributed the greater stability of the chalcogenide to: (1) a substantially lower degradation of the crystal surface via interaction with water and (2) a 7 orders of magnitude lower vacancy migration rate at room temperature. A band gap between 1.75 and 1.94 eV has been experimentally determined for BaZrS₃,[12,20] which is a suitable range for a top subcell augmenting a bottom subcell of Si,[6] copper indium gallium selenide (CIGS),[21] or CdTe[22] in a tandem device. By
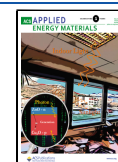
alloying $BaZrS_3$ with Ti or Se, the band gap could even be narrowed to energies suitable for single-junction PV cells.[12,23]

With regard to synthesis methods, the majority of published data so far have concerned bulk material (i.e., powders).[12,24−28] Efforts to grow $BaZrS_3$ single crystals have also been made.[29,30] However, fabrication of thin films of chalcogenide perovskites—a prerequisite for typical optoelectronic devices—remains a challenge to date. Although there are a few examples of $BaZrS_3$ thin films in the literature, industrial-oriented pathways have not been the emphasis yet,[17,20,31−34] as basic problems such as poor microstructure, poor crystallinity, and heavy oxygen contamination still dominate. A recurring issue is that, to achieve good crystallinity or composition, temperature processes in excess of 900 °C have been used, which could hinder the use of $BaZrS_3$ in PV. Conductive rear-contact layers cannot withstand such temperatures under process conditions for chalcogenides, explaining why no solar cell devices have yet been presented. Therefore, it is vital to find methods for $BaZrS_3$ synthesis at lower temperatures. Several reported synthesis routes have been based on sulfurization of $BaZrO_3$ precursors to obtain $BaZrS_3$.[17,20,32] This approach carries the intrinsic issue that oxides are extremely stable compounds and require a high thermal budget to be converted into a sulfide, as noted by Clearfield.[25] It is therefore desirable to avoid synthesis routes that involve oxide precursors. In our previous work, BaS and Zr targets were used to deposit amorphous Ba−Zr−S films by reactive co-sputtering in the presence of H_2S. These precursors were then annealed in an inert atmosphere for crystallization. The optimal temperature to form $BaZrS_3$ was found to be around 900 °C. A related case is the work by Yu et al,[31] who fabricated Ba−Zr−S layers by pulsed laser deposition (PLD). Interestingly, even with a substrate temperature as high as 700 °C in the PLD step, the as-deposited films turned out amorphous and highly sulfur-deficient. To attain stoichiometry and crystallinity, an annealing step of several hours in the presence of CS_2 was necessary. The full width at half-maximum (FWHM) of the 121 X-ray diffraction (XRD) peak decreased from 0.62 to 0.45° with increasing annealing temperatures from 550 to 900 °C, while the S content dropped from ca. 60 to ca. 57%. It is worth noting that most efforts on the growth of $BaZrS_3$ thin films are based on a two-step process, resulting in polycrystalline layers, whereas two works pursued direct epitaxial growth of monocrystalline thin films: Surendran et al. by PLD[33] and Sadeghi et al. by molecular beam epitaxy.[34] Both studies used the FWHM of the 202 peak from a rocking curve to judge crystallization. They report a value of 0.409 and 4° for films grown at 900 and 750 °C, respectively. A noteworthy exception is the work by Ravi et al.[35] As opposed to all aforementioned physical methods, they managed to fabricate ∼50 nm thin films for transistors by solution processing.

In marked contrast to the above results, Wang et al. succeeded in synthesizing $BaZrS_3$ at temperatures as low as 450 °C by solid-state reaction.[36] They also included the additive $BaCl_2$, which had a beneficial effect on $BaZrS_3$ yield, although the mechanism was not determined. Still, they also demonstrated that $BaZrS_3$ can also be obtained without $BaCl_2$ at temperatures down to 500 °C, though in a lesser amount. They demonstrated that an overstoichiometric quantity of S played a crucial role in formation—specifically, a certain, small S excess was required for smooth phase formation at a lower temperature. The addition of too little S led solely to the formation of the binary compounds BaS, BaS_2, and ZrS_2, while a too large S excess produced mainly BaS_3 and ZrS_3. $BaZrS_3$ was formed at a high yield only at intermediate values of S excess, in conjunction with the first appearance of BaS_3. This latter binary compound has a melting point of 554 °C—much lower than that of BaS_2, BaS,[37,38] or any of the Zr−S binaries,[39] which perhaps explains why $BaZrS_3$ synthesis was most effective in the presence of this secondary phase. Thus, formation pathways involving specifically BaS_3 may lead to a better quality ternary phase.[19] If this hypothesis is correct, then a thin-film synthesis could be improved if the conditions for BaS_3 formation are present at some stage of the process. BaS_3 is unlikely to form in the case of a co-sputtered Ba−Zr−S precursor—as in the works by Yu et al.[31] and Comparotto et al.[40]—but it might form as an intermediate phase if the growth starts from binary compounds such as BaS or metals (i.e., Ba). To facilitate this pathway, we have chosen to use Ba−Zr precursors in the present work. With the intention of pursuing an industrial-oriented route, we deposited the metal precursors by magnetron sputtering, which is an easily scalable method suitable for large-scale production. It can provide films of good quality over large areas with high deposition rates and is already employed in mass production in different sectors, including PV.[41] We introduced S in a second step by sulfurization of the metal precursors and investigated the role played by excess S. Since sputtering and sulfurization took place in two different systems, measures had to be taken to avoid air exposure of the Ba−Zr films during sample transport. To this end, a SnS-capping layer was deposited in situ on top of the Ba−Zr precursors, to minimize excessive oxidation. SnS was chosen since it can be sputter-deposited in the same chamber used for Ba−Zr deposition, and since its relatively low evaporation temperature should enable it to be thermally removed at the beginning of the subsequent sulfurization process. This procedure was effective in avoiding excessive oxygen contamination, although a small amount of undesired Sn was still present at the surface in the final samples. With this approach, we were able to synthesize $BaZrS_3$ thin films on metal back contacts below 600 °C. The FWHM of the 121 XRD peak is comparable to, or even lower than, that obtained by other synthesis approaches that required at least 900 °C.[31,40] Our results are discussed in the context of the above reaction chemistry.

2. RESULTS AND DISCUSSION

Precursors consisted of the following structure of stacked layers: Si/Mo/Ba−Zr/SnS. The thickness of SnS was approximately 100 nm thick. A detailed study of the capping layer is described in the Supporting Information (SI).

In one case, no SnS-capping layer was deposited on a Si/Mo/Ba−Zr sample, which was then sulfurized with the S source at 135 °C. An O content of around 50% was measured after sulfurization, and no peaks belonging to $BaZrS_3$ were detected by XRD (not shown). From these observations, two main conclusions can be drawn:

(1) If Ba−Zr precursors are exposed to air between sputtering and sulfurization, even for a fraction a minute, a capping layer is necessary to avoid oxidation;

(2) A large amount of O in the precursor hinders the formation of $BaZrS_3$.

The precursors were sulfurized to investigate the formation of $BaZrS_3$ in presence of excess S. The temperature of the S
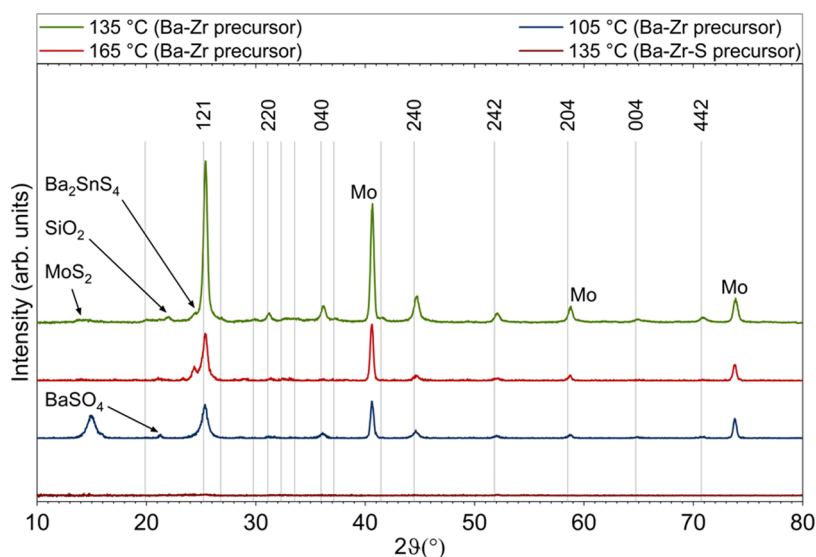
Figure 1. Grazing-incidence X-ray diffraction (GI-XRD) patterns measured on compositionally graded Si/Mo/Ba−Zr/SnS samples sulfurized with the S source at 105, 135, and 165 °C. The three patterns exhibit the lowest FWHM of the 121 reflection peak measured for each temperature, as presented also in Figure 2a. A Si/Ba−Zr−S precursor sulfurized with the S source at 135 °C is also shown for comparison. Lines and Miller indices come from the reference pattern for BaZrS$_3$ of Clearfield et al.[25] Peaks belonging to the Mo layer or other compounds are labeled.
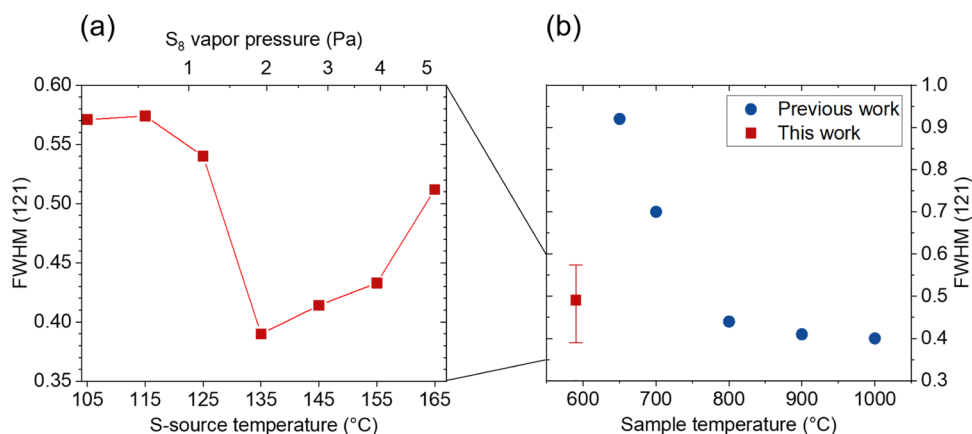

Figure 2. (a) Lowest FWHM of the 121 reflection peak obtained for each S source temperature and corresponding vapor pressure. (b) FWHM of the 121 reflection peak as a function of sample temperature, where mean, maximum and minimum of all investigated S source temperatures in the present paper are compared with the results from our previous work. Reproduced from Comparotto, C.; Davydova, A.; Ericson, T.; Riekehr, L.; Moro, M. V.; Kubart, T.; Scragg, J. Chalcogenide Perovskite BaZrS$_3$: Thin-Film Growth by Sputtering and Rapid Thermal Processing. ACS Appl. Energy Mater. 2020, 3, 2762−2770. Copyright 2020 American Chemical Society.

source was varied in seven different runs to examine the role of S vapor pressure during the annealing step. While the sample temperature was in the range of 550−590 °C, the S source was kept constant at a series of temperatures from 105 to 165 °C— at intervals of 10 °C and with an accuracy of ± 1 °C—during the sulfurization process. These temperatures can be roughly converted into partial pressures of S$_8$ covering the approximate range of 0.1−5 Pa (see the SI for the calculation).

The XRD analysis of the sample sulfurized with the S source at 135 °C, presented in Figure 1 by the green curve, confirms that BaZrS$_3$ is the main phase. Besides the intense peaks related to the Mo back contact, three minor peaks are also present, which are attributed to Ba$_2$SnS$_4$ (see later), MoS$_2$, and SiO$_2$. For comparison, the XRD curves for the two extreme conditions—i.e., the S source heated to 105 or 165 °C—are also plotted in Figure 1. Clearly, the peaks belonging to BaZrS$_3$ are much less intense and broader in these cases.

The FWHM of the 121 reflection peak of BaZrS$_3$ was calculated from XRD measurements on several spots on the compositionally graded samples, ranging from the most Ba-rich to the most Zr-rich region. Since a large variation was often observed, only the lowest FWHM for each temperature was considered for the plot in Figure 2a to highlight the highest degree of crystallinity achieved in each case. An FWHM lower than 0.45 °C was achieved with the S source between 135 and 155 °C, corresponding to an approximate S$_8$ vapor pressure in the range of 2−4 Pa. Lower or higher temperatures rapidly increased the FWHM of the 121 reflection peak above 0.5°.

The mean, maximum, and minimum FWHM from this series are also plotted in red in Figure 2b versus the temperature of the sample, and compared with the results from our previous paper.[40] In this work, the sample temperature was fixed at 590 °C, whereas in our previous paper, it ranged from 650 to 1000 °C. It emerges that, for any investigated S source temperature, the new process route

delivered $BaZrS_3$ thin films of higher crystalline quality compared with the old approach—where no excess S was added during annealing—for a sample temperature of 700 °C or lower. The lowest FWHM reached with the new process was even lower than the lowest achieved at 900−1000 °C in the S-free method.

To investigate whether the improvement in crystallization is coupled with the precursor type or the presence of excess S in the thermal process, a sulfur-containing precursor—i.e., Ba−Zr−S—was processed with the present method, using an S source temperature of 135 °C. The fabrication procedure of this precursor is described in detail in our previous work.[40] Grazing-incidence X-ray diffraction (GI-XRD) was then performed. Interestingly, no peaks were detected (Figure 1), meaning that the film was still amorphous. It follows that, apart from the presence of excess S during the process, the nature of the precursor is also fundamental.

To evaluate the role of O and Sn impurities in the process, the O and Sn concentrations in the samples were compared for the different tested temperatures of the S source. [O] and [Sn] were, respectively, calculated as $\frac{O}{Ba + Zr + S + O}$ and $\frac{Sn}{Ba + Zr + S + Sn}$ from scanning electron microscopy with energy-dispersive spectroscopy (SEM−EDS) and plotted in Figure 3.
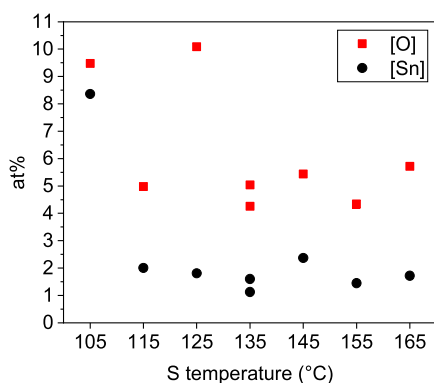

Figure 3. [O] and [Sn] from SEM−EDS as a function of S source temperature.

In terms of the degree of contamination, this seems relatively constant for an S source temperature of 115 °C or higher: [O] and [Sn] minimally fluctuate around 5 and 2 atom %, respectively. Only for 125 °C, an oxygen concentration of around 10% was observed. This measurement point could be an outlier, for instance, operator related, especially when transporting the sample from the sputtering system to the sulfurization furnace. When the sample was sulfurized with the

S source at 105 °C; however, both [O] and [Sn] deviate significantly from the rest of the data points. In this case, it is plausible that the lack of available S influenced the overall chemical reaction. Since the impurity content did not vary strongly for most of the range, we can therefore conclude that O and Sn impurities did not significantly affect the investigated FWHM of the 121 reflection peak. We note that the final sulfurized films contained a similar O concentration to that found in our previous publication.[40]

Our results provide some useful insight into the formation process of $BaZrS_3$. In qualitative agreement with Wang et al. for a very different type of process,[36] the behavior seen in Figure 2a confirms that a certain, defined S excess is required for smooth phase formation at moderate temperatures when starting from elemental precursors. This highlights the key role played by the S vapor pressure during the crystallization of $BaZrS_3$. The hypothesis outlined in the introduction, that the reaction route depends on S excess because the nature of the intermediate phases is changed, is in superficial agreement with our results. Specifically, the low melting point phase BaS_3[37,38] is expected to form at intermediate S pressure, while the $BaZrS_3$ phase is supposed to decompose at too great an S excess.[19] It is possible that we are seeing this behavior in Figure 2a, although since secondary phases were not observed in the final films, we cannot yet confirm the role of BaS_3.

Regardless of the nature of intermediate phases, the importance of the reaction pathway is made very clear by the observation that already sulfur-containing Ba−Zr−S precursors completely failed to crystallize under the same reaction conditions as Ba−Zr precursors. The formation of any intermediate phases would be unlikely in the former precursor type; direct crystallization would be expected instead. The difference in diffusivity of elements in the two different precursor types, by virtue of an intermediate phase appearing in a given range of S pressures, could explain the extreme differences in crystallization behavior observed here. Future studies should focus on elucidating the reaction mechanism more clearly since such details clearly affect the prospects for integrating $BaZrS_3$ into devices.

We now turn our attention to the evolution of microstructure and the influence of the SnS cap on $BaZrS_3$ layer formation. To get insight into the depth distribution of the elements, scanning transmission electron microscopy (STEM) was performed on cross sections of a compositionally graded sample sulfurized with the S source at 145 °C. From SEM−EDS measurements, $\frac{Ba}{Ba + Zr}$ varied from 0.42 to 0.60 over a distance of ca. 70 mm, while the S content was in the range of 59−61%. Figure 4 shows four annular dark-field (ADF) images
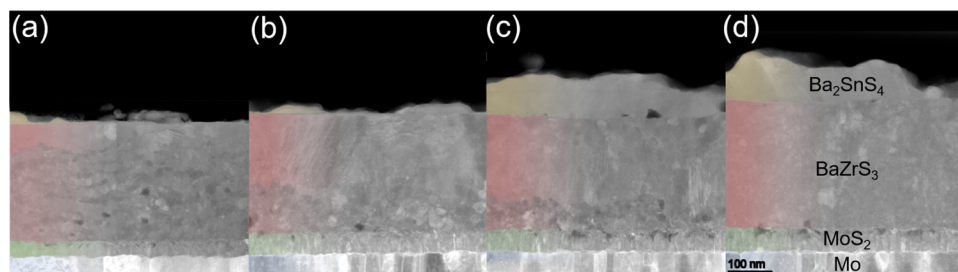

Figure 4. STEM-ADF cross sections of a sample sulfurized with the S source kept at 145 °C, measured progressively on (a) the most Zr-rich side, (b) a slightly Zr-rich area, (c) a slightly Ba-rich area and (d) the most Ba-rich side. The thickness of the $BaZrS_3$ layer is ca. 300 nm.
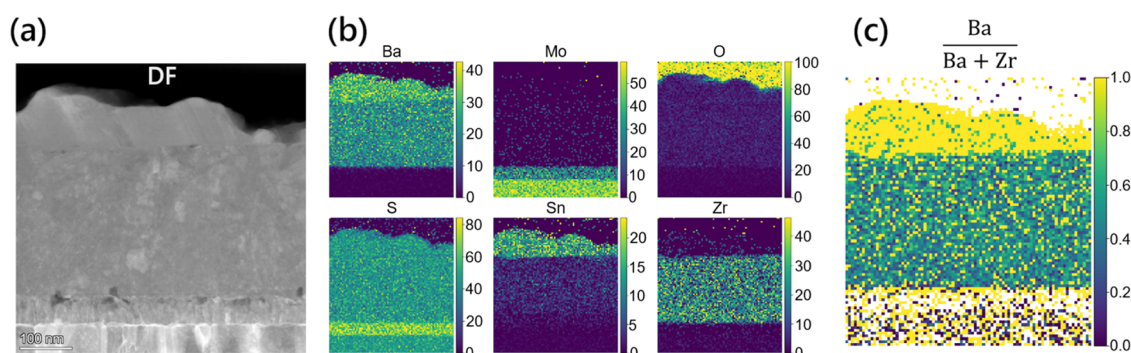
Figure 5. (a) STEM-ADF cross section of a sulfurized sample with the S source at 145 °C, measured on the most Ba-rich side. (b) Relative EDS maps displaying the composition of the most relevant elements in atom %$_{rel}$. (c) Combined map showing the ratio $\frac{Ba}{Ba + Zr}$.
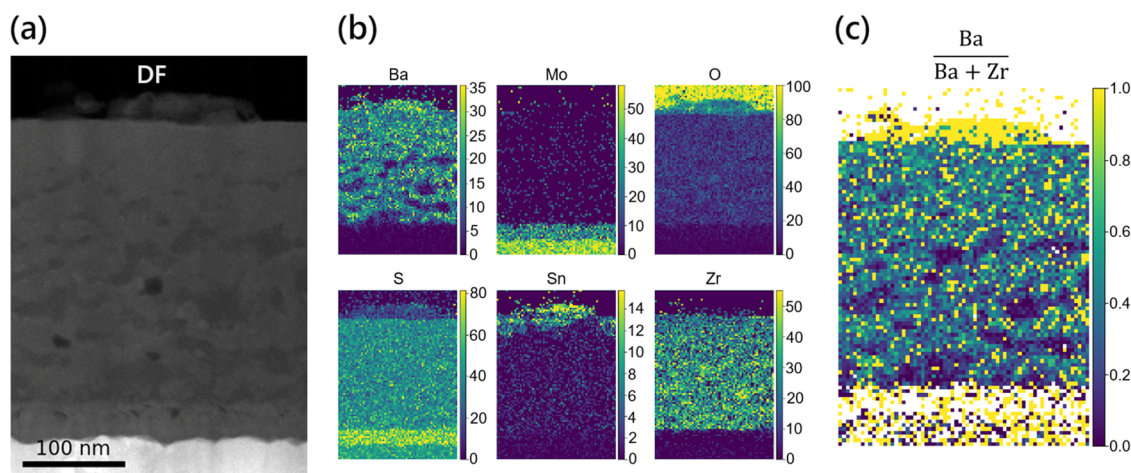

Figure 6. (a) STEM-ADF cross section of a sample sulfurized with the S source heated to 145 °C, measured on the most Zr-rich side. (b) Relative EDS maps displaying the composition of the most relevant elements in atom %$_{rel}$. (c) Combined map showing the ratio $\frac{Ba}{Ba + Zr}$.

measured progressively from the Zr-rich side (a) to the Ba-rich side (d).

Unexpectedly, a layer of large particles formed on the top surface, with increasing thickness and density toward the Ba-rich side of the compositionally graded sample, becoming clearly visible in Figure 4c,d. STEM-EDS maps, presented in Figure 5b, were performed on the most Ba-rich position to investigate the elemental composition of this top layer. They show that Ba, Sn, and S are the major constituents, which suggests that the SnS cap reacted with Ba during the sulfurization step. By exclusion, the best match for this compound from our XRD analysis is Ba_2SnS_4 (Figure 1). This undesired reaction consumed part of the Ba that was intended to create the perovskite layer instead. Figure 5b also shows that Sn remained confined at the surface and that the 40−50 nm thin layer between the Mo back contact and the perovskite has the expected composition of MoS_2. In view of making solar cell devices in the future, this thin film is not expected to be detrimental.[42]

Turning to the $BaZrS_3$ perovskite layer itself, its thickness does not significantly depend on the position on the compositionally graded sample, being ca. 300 nm in all four cross sections shown in Figure 4. However, the microstructure is position-dependent. In Figure 4a, a bilayer is visible in each location, the top part being more homogeneous and denser, and the bottom part is composed of much smaller and more irregular grains. The upper region is only 40−50 nm thick on

the most Zr-rich side of the sample (Figure 4a), but it extends more and more when moving toward the Ba-rich side, until the whole $BaZrS_3$ film appears uniform, as observable in Figure 4d.

To analyze more closely the inhomogeneous microstructure of the $BaZrS_3$ film in the most Zr-rich region of the sample, a combined STEM-EDS map representing the ratio $\frac{Ba}{Ba + Zr}$ was constructed and is presented in Figure 6c. Clearly, the metals are much more homogeneously distributed in the top region of the $BaZrS_3$ layer, while in the lower part, several relatively large spots seem to completely lack Ba. The bilayer structure seems to be simply related to the metal stoichiometry at different points in the sample. The depth-wise composition gradient appears to arise during the sulfurization process. This can be explained by a phase separation process induced by local nonstoichiometry or unequal diffusion rates of the metal elements, coupled with the fact that S vapor arrives only from the surface direction. Based on the observation that the top material partly consumes some Ba, the ideal composition for forming $BaZrS_3$ in the main layer was presumably found toward the Ba-rich side of the sample. Indeed, the most homogeneous microstructure as well as an even composition throughout the perovskite layer is found in Figure 4d, i.e., on the most Ba-rich side.

To obtain compositional depth profiles over a large spot size in the order of a few square millimeters, two ion beam analysis techniques, Rutherford backscattering spectrometry (RBS) and coincidence time-of-flight/energy elastic recoil detection
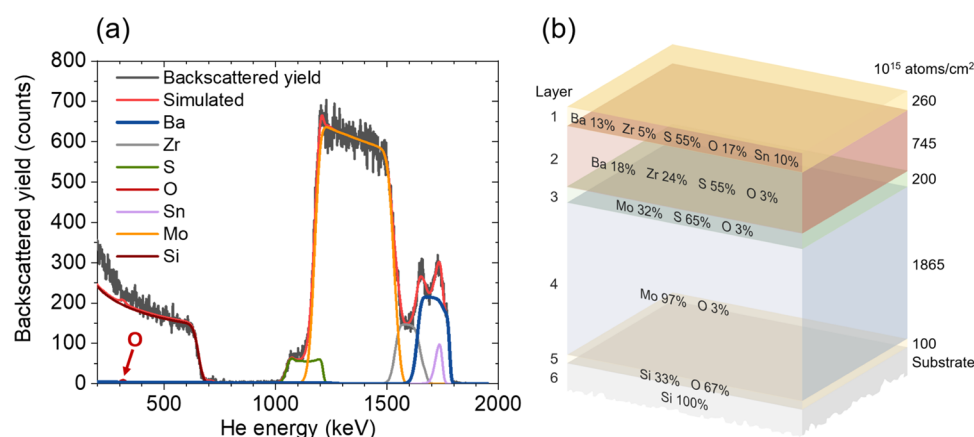
Figure 7. (a) RBS spectra and simulated curve of a sample sulfurized with the S source at 135 °C. (b) Elemental composition and thickness of the six layers used for the fit.
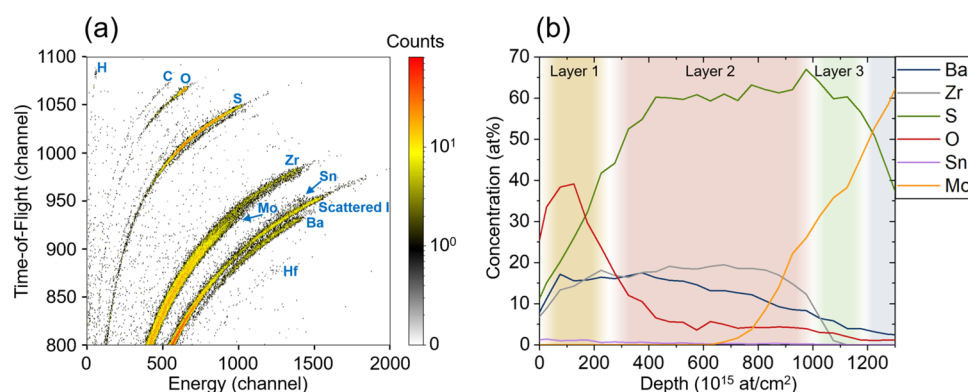

Figure 8. (a) ToF-ERDA spectra of a sample sulfurized with the S source at 135 °C and (b) the corresponding calculated depth profiles. The layers used in SIMNRA to simulate the RBS spectra are overlapped by regions of different colors.

analysis (ToF-ERDA), were performed on a sample sulfurized with the S source at 135 °C. Based on SEM−EDS, a spot where Ba:Zr was 1:1 was aimed for the IBA measurements. The RBS spectrum recorded for the incident angle of 5° is shown in Figure 7a by the gray curve. Using the SIMNRA code,[43] the experimental spectrum was fitted and is shown in the same figure by the red curve, while the other colors depict the fits of the single elements. Note that these fits already contain information from ToF-ERDA, as a result of an iterative data analysis procedure (see Moro et al. for further details[44]). Six layers, including the Si substrate, were used to fit the experimental spectrum with good approximation. The elemental composition of each layer and their thickness—expressed in units of 10^{15} at cm^{-2}—are shown in Figure 7b.

According to the RBS analysis, Sn reacts with the surface of the precursor to form an undesired layer, but its diffusion towards the substrate is limited, corroborating what is seen by STEM-EDS (Figure 5b). The near-surface material (top ca. 50 nm) also contains a significant amount of O, which is otherwise estimated to be around 3% in the underlying material. The second layer corresponds to the BaZrS$_3$ perovskite, although slightly off-stoichiometric, which can be attributed to the fact that the top layer consumed some Ba, as discussed above. Assuming a bulk density of 4.22 g cm^{-3} for BaZrS$_3$, an approximate thickness of 200 nm is estimated from the RBS measurements, though the actual mass density could be lower in the case of a porous synthesized film, which would then be thicker. The third and fourth layers have the expected

composition of MoS$_2$ and Mo, with the inclusion of a small amount of O impurity. We note that the XRD as well as the STEM-EDS and the RBS results demonstrate that the conductive Mo layer remains intact after the formation process of BaZrS$_3$. A few nanometers of SiO$_2$ had to be included on top of the Si substrate to improve the fit of the recorded RBS spectra, which is in line with that observed by XRD (Figure 1).

The ToF-ERDA raw data and depth profiles calculated using Potku[45] are shown in Figure 8a,b, respectively. They reaffirm that Sn diffusion toward the substrate is limited and that Sn is not detectable in the perovskite layer, although the Sn fraction is underestimated by ToF-ERDA, as Sn recoils cannot be well separated from scattered I particles from the primary beam. While the second layer appeared S-poor in RBS, the depth profiles from ToF-ERDA—which can detect light elements with greater sensitivity than the former technique—show that [S] is actually around 60% here. In addition, the Ba and Zr profiles—depicted by the blue and gray lines, respectively—corroborate what observed so far: The top layer deprived the perovskite bulk (layer 2) of some Ba. Note that a benign artifact from the data analysis with Potku yields depth profiles that sum to more than 100% at large depths (apparent near the Mo layer interface). This is due to a combination of multiple scattering and sample surface roughness, which introduce inaccuracy in the model of single scattering for a planar surface used by the conversion algorithm. Surface roughness, along with the 300 ps resolution of the flight time detector used for the measurement, also limits depth resolution and results in

interfaces that appear smeared out compared to the sharp layer limits depicted in Figure 7b. This is particularly apparent here at the Mo film interface—where the allocation of counts to regions of interest gives some misattribution of Mo as Zr and vice versa anyway. The discrepancy between the two IBA techniques in Zr and Sn fractions near the surface is most likely attributed to the inhomogeneous nature of the top layer; its thickness and composition can have been significantly different on the two measured spots. The much larger O concentration in the first layer is instead attributed to the fact that ToF-ERDA was performed 7 months after RBS, giving time to the material at the surface to oxidize during storage in air. Interestingly, the O fraction in the second layer is still around 5%, confirming the great long-term stability of $BaZrS_3$. As an aside, it is interesting to note that ToF-ERDA was even capable of detecting Hf, as visible in Figure 8a, although it was too little to be quantified. Its presence in the Zr target can be therefore confirmed.

3. CONCLUSIONS

$BaZrS_3$ is expected to exhibit excellent optoelectronic properties, comparable to or even better than those of halide perovskites such as $MAPbI_3$, but with the asset of being extremely chemically robust and nontoxic. In this work, we report the first thin-film synthesis of $BaZrS_3$ on metal back contacts, using a sputter-sulfurization approach with process temperature below 600 °C. We evaluated the influence of S partial pressure on the process, with our results suggesting that the reaction pathway—decided by the combination of S pressure and precursor composition—is of fundamental importance for determining how the perovskite phase crystallizes. A thin SnS cap was deposited on the co-sputtered metal precursors to prevent excessive oxidation. TEM and ion beam analysis indicate an undesired reaction with the precursor that modified the composition of the underlying perovskite layer. Despite this, the crystalline quality of the $BaZrS_3$ film, based on XRD analysis, is comparable to or even better than that achieved with different synthesis routes that require a much higher thermal budget. The role played by S excess and the intermediate secondary phase BaS_3 during the high-temperature step should be taken into consideration in future works. Sulfurization at temperatures lower than 600 °C also merits further investigation.

Since separate sputtering and sulfurization systems were used in the present work, it was necessary to protect the metal precursors with a capping layer to avoid excessive oxidation during the transport. In an ideal sputter-sulfurization approach, no cap would be needed. This condition could be achieved if the vacuum was not broken between the two processes, or if the precursors were at least not exposed to air during transport. Under these circumstances, only $BaZrS_3$ is expected to form on top of the Mo back contact, with the exception of a very thin MoS_2 layer in between, which should not be detrimental for solar cell applications.[42] The $BaZrS_3$ thin film, synthesized with such an industrial-oriented pathway, would be free from additional material on the surface and could then be further characterized optically and electrically to assess the photovoltaic potential of this chalcogenide perovskite.

4. EXPERIMENTAL SECTION/METHODS

4.1. Sample Preparation. An ca. 300 nm thick Mo film was initially deposited on Cz–Si wafers by pulsed direct current (DC) sputtering in a Von Ardenne system from a 99.95% pure metal target.

Afterward, Ba and Zr were co-sputtered in a Kurt J. Lesker system with a base pressure in the order of 10^{-5} Pa. The Ba and Zr metal targets were 99.5 and 99.7% pure (excluding Hf), respectively. Both targets had a diameter of 7.62 cm (3 in.) and were manufactured by Plasmaterials, Inc. The depositions took place in Ar atmosphere (purity of the source: 99.9997%) at 0.57 Pa. The Ba target was powered by radio frequency (RF) mode with a power density of 0.81 W cm^{-2}, while the Zr target by pulsed DC with 0.99 W cm^{-2}. During the co-deposition of Ba and Zr, the samples were rotated only for the study of the capping layer described in the SI, not for the fabrication of $BaZrS_3$. In this way, compositionally graded thin films were obtained after sulfurization, i.e., from Ba-poor to Ba-rich, to explore the influence of stoichiometry on the formation of $BaZrS_3$. Due to the instantaneous reaction of Ba with ambient air, it was not possible to measure the thickness of as-deposited Ba–Zr layers on cross sections by profilometry or SEM. Instead, ToF-ERDA was performed on a capped sample that had been exposed to air only for very few minutes. The O concentration within the measured Ba–Zr layer was 6.6%, confirming that the sample had not significantly oxidized. Assuming a mass density of 3.5 and 6.5 g cm^{-3} for Ba and Zr, respectively, as if they were two separate films, a thickness of around 100 nm is estimated for a dense Ba–Zr layer, which could obviously be larger if the material was porous. It is worth noting that, after initial installation, the Ba target had to be presputtered for a couple of hours to remove the oxidized surface—which resulted in a clear change in plasma color from purple to green. Subsequently, minor oxidation from the background pressure, occurring over a period of days, could be sputtered away within a few minutes, with a clear change in the target potential marking the end-point.

Directly after Ba and Zr, a SnS-capping layer was deposited in the same chamber by pulsed DC sputtering in Ar atmosphere at 0.57 Pa. The power was 0.55 W cm^{-2}, and the SnS target (Pioneer Materials, Inc.) had a diameter of 7.62 cm (3 in.). To study the effect of the capping layer (see the SI), the deposition time was varied from 0 to 30 min. To circumvent the challenge of measuring the thickness of the cap on top of an uneven, oxidized Ba–Zr layer, SnS was also directly deposited on a Si witness piece, and SEM measurements were performed on cross sections. Assuming a similar growth rate on Si and Ba–Zr, the investigated thickness range was 0–200 nm. For the fabrication of $BaZrS_3$ thin films, a 100 nm thick cap was intended. Sample rotation was used during all depositions of SnS to uniformly coat the compositionally graded Ba–Zr films. All of the above-mentioned depositions took place at ambient temperature.

For sulfurization, the as-sputtered samples were processed in a custom-made tube furnace with an approximate volume of 15 L and a base pressure in the order of 0.1–1 Pa. For the majority of the runs, the sample was placed on an open graphite holder, while S-powder was loaded into a separate small vessel, being the S source. Both the S source and the sample were inserted in a load lock, which was then pumped to remove traces of air before beginning the sulfurization process. By means of a rod and a vacuum feedthrough, the S source was transferred toward the hot zone of the preheated furnace. By changing the distance of the S-containing vessel from the heating zone, it is possible to control the temperature of S at the source— and thereby the equilibrium vapor pressure. Once the vessel reached the desired temperature, the sample was transferred into the hot zone of the furnace by a second rod via another vacuum feedthrough. For all runs, the temperature of the furnace was set to 600 °C. Upon insertion, the sample holder reached 550 °C within a few minutes, after which the sample remained in the hot zone for 20 min. During this period, Ar was continuously flowed at 50 sccm, the pressure inside the tube was max. 80 Pa, and the S source was kept within a margin of ±1 °C from the set temperature. By the end of the dwell step, the samples reached ca. 590 °C. Finally, both sample and S source were slowly pulled away from the heating zone and allowed to cool to below 70 °C before unloading. The S source was weighed before and after the process to determine the evaporated quantity, which was then converted into an average S pressure during the run— see the SI. For the study on the capping layer described in the SI, the S source temperature was always 135 °C, while seven values between

105 and 165 °C were tested in different runs to investigate the effect of S vapor pressure on the formation of $BaZrS_3$ thin films. In one case (see SI), for comparison, a sample was loaded together with 420.4 mg of S into a closed graphite box. The separate S source was not used this time, but the process was otherwise identical, and all of the S-powder evaporated during the sulfurization process.

4.2. Characterization. Elemental analysis was performed by EDS at 10 keV in a Zeiss LEO 1550 SEM with an EDAX EDS system.

GI-XRD was performed in a SIEMENS D5000 system with parallel beam geometry at 45 keV with Cu Kα radiation (λ = 1.5406 Å) at a 1° incident angle. The K$_{\alpha 2}$ component and the background were computationally subtracted from the raw diffraction pattern in HighScore Plus by PANalytical.[46]

The transmission electron microscopy analyses were conducted on a Titan Themis 200 (FEI) equipped with a SuperEDS detector (Oxford). The energy-dispersive X-ray spectroscopy (EDS) analyses were acquired using Esprit (Bruker), and the data were processed using Hyperspy (v1.64). The TEM lamellae were carefully prepared by focused ion beam using a StrataDB235 (FEI) and a Crossbeam 550 (Zeiss) and systematically polished using an ion accelerating voltage below 5 kV at the final stage.

Composition depth profiles for the thin film as well as the back contact layer were obtained by ToF-ERDA and RBS. For the former method, a 44 MeV beam of $^{127}I^{10+}$ was employed, with 22.5° incoming and exit angles with respect to the sample surface. Recoils were detected with the system described in ref 47 at 45°. In the case of RBS, the probing beam consisted of 2 MeV $^4He^+$ impinging on the sample at an angle of 5° with respect to the surface normal. Backscattered ions were detected at a scattering angle of 170 and a 5° exit angle. The sample was randomly wiggled within a 2° angle interval around this starting position during data acquisition as a standard measure to average out possible ion channeling effects.

ASSOCIATED CONTENT

Ⓢ Supporting Information

The Supporting Information is available free of charge at https://pubs.acs.org/doi/10.1021/acsaem.2c00704.

Thickness and performance of the SnS-capping layer (S1); oxygen contamination (S1.1); evaporation of the SnS-capping layer (S1.2); calculation of average S pressure during the thermal process (S2); and fabrication of $BaZrS_3$ films at a high pressure (S3) (PDF)

AUTHOR INFORMATION

Corresponding Author

Corrado Comparotto − *Division of Solar Cell Technology, Department of Materials Science and Engineering, Uppsala University, Uppsala 75237, Sweden;* ● orcid.org/0000-0002-6020-0771; Email: corrado.comparotto@angstrom.uu.se

Authors

Petter Ström − *Division of Applied Nuclear Physics, Department of Physics and Astronomy, Uppsala University, Uppsala 75237, Sweden*

Olivier Donzel-Gargand − *Division of Solar Cell Technology, Department of Materials Science and Engineering, Uppsala University, Uppsala 75237, Sweden;* ● orcid.org/0000-0002-2101-3746

Tomas Kubart − *Division of Solid State Electronics, Department of Electrical Engineering, Uppsala University, Uppsala 75237, Sweden*

Jonathan J. S. Scragg − *Division of Solar Cell Technology, Department of Materials Science and Engineering, Uppsala University, Uppsala 75237, Sweden;* ● orcid.org/0000-0001-8686-8721

Complete contact information is available at:
https://pubs.acs.org/10.1021/acsaem.2c00704

Notes

The authors declare no competing financial interest.

REFERENCES

(1) Singh, R. Why Silicon Is and Will Remain the Dominant Photovoltaic Material. *J. Nanophotonics* **2009**, 3, No. 032503.

(2) International Technology Roadmap for Photovoltaic. *ITRPV: Large Format Wafer Preferred, But More Development Work Required*; ITRPV, 2021.

(3) Kerr, M. J.; Cuevas, A.; Campbell, P. Limiting Efficiency of Crystalline Silicon Solar Cells Due to Coulomb-Enhanced Auger Recombination. *Prog. Photovoltaics* **2003**, 11, 97−104.

(4) Richter, A.; Hermle, M.; Glunz, S. W. Reassessment of the Limiting Efficiency for Crystalline Silicon Solar Cells. *IEEE J. Photovoltaics* **2013**, 3, 1184−1191.

(5) Yamamoto, K.; Yoshikawa, K.; Uzu, H.; Adachi, D. High-Efficiency Heterojunction Crystalline Si Solar Cells. *Jpn. J. Appl. Phys.* **2018**, 57, No. 08RB20.

(6) Werner, J.; Niesen, B.; Ballif, C. Perovskite/Silicon Tandem Solar Cells: Marriage of Convenience or True Love Story?—An Overview. *Adv. Mater. Interfaces* **2018**, 5, No. 1700731.

(7) Green, M. A.; Dunlop, E. D.; Hohl-Ebinger, J.; Yoshita, M.; Kopidakis, N.; Hao, X. Solar Cell Efficiency Tables (Version 58). *Prog. Photovoltaics* **2021**, 29, 657−667.

(8) Krishnan, U.; Kaur, M.; Kumar, M.; Kumar, A. Factors Affecting the Stability of Perovskite Solar Cells: A Comprehensive Review. *J. Photon. Energy* **2019**, 9, No. 021001.

(9) Berhe, T. A.; Su, W.-N.; Chen, C.-H.; Pan, C.-J.; Cheng, J.-H.; Chen, H.-M.; Tsai, M.-C.; Chen, L.-Y.; Dubale, A. A.; Hwang, B.-J. Organometal Halide Perovskite Solar Cells: Degradation and Stability. *Energy Environ. Sci.* **2016**, 9, 323−356.

(10) Wani, A. L.; Ara, A.; Usmani, J. A. Lead Toxicity: A Review. *Interdiscip. Toxicol.* **2015**, 8, 55−64.

(11) Sun, Y.-Y.; Agiorgousis, M. L.; Zhang, P.; Zhang, S. Chalcogenide Perovskites for Photovoltaics. *Nano Lett.* **2015**, 15, 581−585.

(12) Nishigaki, Y.; Nagai, T.; Nishiwaki, M.; Aizawa, T.; Kozawa, M.; Hanzawa, K.; Kato, Y.; Sai, H.; Hiramatsu, H.; Hosono, H.; Fujiwara, H. Extraordinary Strong Band-Edge Absorption in Distorted Chalcogenide Perovskites. *Sol. RRL* **2020**, 4, No. 1900555.

(13) Perera, S.; Hui, H.; Zhao, C.; Xue, H.; Sun, F.; Deng, C.; Gross, N.; Milleville, C.; Xu, X.; Watson, D. F.; Weinstein, B.; Sun, Y.-Y.; Zhang, S.; Zeng, H. Chalcogenide Perovskites—an Emerging Class of Ionic Semiconductors. *Nano Energy* **2016**, 22, 129−135.

(14) Niu, S.; Milam-Guerrero, J.; Zhou, Y.; Ye, K.; Zhao, B.; Melot, B. C.; Ravichandran, J. Thermal Stability Study of Transition Metal Perovskite Sulfides. *J. Mater. Res.* **2018**, 33, 4135−4143.

(15) Ju, M.-G.; Dai, J.; Ma, L.; Zeng, X. C. Perovskite Chalcogenides with Optimal Bandgap and Desired Optical Absorption for Photovoltaic Devices. *Adv. Energy Mater.* **2017**, *7*, No. 1700216.

(16) Huo, Z.; Wei, S.-H.; Yin, W.-J. High-Throughput Screening of Chalcogenide Single Perovskites by First-Principles Calculations for Photovoltaics. *J. Phys. D: Appl. Phys.* **2018**, *51*, No. 474003.

(17) Wei, X.; Hui, H.; Zhao, C.; Deng, C.; Han, M.; Yu, Z.; Sheng, A.; Roy, P.; Chen, A.; Lin, J.; Watson, D. F.; Sun, Y.-Y.; Thomay, T.; Yang, S.; Jia, Q.; Zhang, S.; Zeng, H. Realization of BaZrS$_3$ Chalcogenide Perovskite Thin Films for Optoelectronics. *Nano Energy* **2020**, *68*, No. 104317.

(18) Xu, J.; Fan, Y.; Tian, W.; Ye, L.; Zhang, Y.; Tian, Y.; Han, Y.; Shi, Z. Enhancing the Optical Absorption of Chalcogenide Perovskite BaZrS$_3$ by Optimizing the Synthesis and Post-Processing Conditions. *J. Solid State Chem.* **2022**, *307*, No. 122872.

(19) Sopiha, K. V.; Comparotto, C.; Márquez, J. A.; Scragg, J. J. S. Chalcogenide Perovskites: Tantalizing Prospects, Challenging Materials. *Adv. Opt. Mater.* **2022**, *10*, No. 2101704.

(20) Gupta, T.; Ghoshal, D.; Yoshimura, A.; Basu, S.; Chow, P. K.; Lakhnot, A. S.; Pandey, J.; Warrender, J. M.; Efstathiadis, H.; Soni, A.; Osei-Agyemang, E.; Balasubramanian, G.; Zhang, S.; Shi, S.-F.; Lu, T.-M.; Meunier, V.; Koratkar, N. An Environmentally Stable and Lead-Free Chalcogenide Perovskite. *Adv. Funct. Mater.* **2020**, *30*, No. 2001387.

(21) Song, Z.; Chen, C.; Li, C.; Awni, R. A.; Zhao, D.; Yan, Y. Wide-Bandgap, Low-Bandgap, and Tandem Perovskite Solar Cells. *Semicond. Sci. Technol.* **2019**, *34*, No. 093001.

(22) Rühle, S. The Detailed Balance Limit of Perovskite/Silicon and Perovskite/CdTe Tandem Solar Cells. *Phys. Status Solidi A* **2017**, *214*, No. 1600955.

(23) Wei, X.; Hui, H.; Perera, S.; Sheng, A.; Watson, D. F.; Sun, Y.-Y.; Jia, Q.; Zhang, S.; Zeng, H. Ti-Alloying of BaZrS$_3$ Chalcogenide Perovskite for Photovoltaics. *ACS Omega* **2020**, *5*, 18579–18583.

(24) Hahn, H.; Mutschke, U. Untersuchungen über ternäre Chalkogenide. XI. Versuche zur Darstellung von Thioperowskiten. *Z. Anorg. Allg. Chem.* **1957**, *288*, 269–278.

(25) Clearfield, A. The Synthesis and Crystal Structures of Some Alkaline Earth Titanium and Zirconium Sulfides. *Acta Crystallogr.* **1963**, *16*, 135–142.

(26) Lelieveld, R.; IJdo, D. J. W. Sulphides with the GdFeO$_3$ Structure. *Acta Crystallogr., Sect. B: Struct. Sci.* **1980**, *36*, 2223–2226.

(27) Niu, S.; Huyan, H.; Liu, Y.; Yeung, M.; Ye, K.; Blankemeier, L.; Orvis, T.; Sarkar, D.; Singh, D. J.; Kapadia, R.; Ravichandran, J. Bandgap Control via Structural and Chemical Tuning of Transition Metal Perovskite Chalcogenides. *Adv. Mater.* **2017**, *29*, No. 1604733.

(28) Filippone, S.; Song, S.; Jaramillo, R. High Densification of BaZrS$_3$ Powder Inspired by the Cold-Sintering Process. *J. Mater. Res.* **2021**, *36*, 4404–4412.

(29) Niu, S.; Zhao, B.; Ye, K.; Bianco, E.; Zhou, J.; McConney, M. E.; Settens, C.; Haiges, R.; Jaramillo, R.; Ravichandran, J. Crystal Growth and Structural Analysis of Perovskite Chalcogenide BaZrS$_3$ and Ruddlesden–Popper Phase Ba$_3$Zr$_2$S$_7$. *J. Mater. Res.* **2019**, *34*, 3819–3826.

(30) Li, W.; Niu, S.; Zhao, B.; Haiges, R.; Zhang, Z.; Ravichandran, J.; Janotti, A. Band Gap Evolution in Ruddlesden-Popper Phases. *Phys. Rev. Mater.* **2019**, *3*, No. 101601.

(31) Yu, Z.; Wei, X.; Zheng, Y.; Hui, H.; Bian, M.; Dhole, S.; Seo, J.-H.; Sun, Y.-Y.; Jia, Q.; Zhang, S.; Yang, S.; Zeng, H. Chalcogenide Perovskite BaZrS$_3$ Thin-Film Electronic and Optoelectronic Devices by Low Temperature Processing. *Nano Energy* **2021**, *85*, No. 105959.

(32) Márquez, J. A.; Rusu, M.; Hempel, H.; Ahmet, I. Y.; Kölbach, M.; Simsek, I.; Choubrac, L.; Gurieva, G.; Gunder, R.; Schorr, S.; Unold, T. BaZrS$_3$ Chalcogenide Perovskite Thin Films by H$_2$S Sulfurization of Oxide Precursors. *J. Phys. Chem. Lett.* **2021**, *12*, 2148–2153.

(33) Sadeghi, I.; Ye, K.; Xu, M.; Li, Y.; LeBeau, J. M.; Jaramillo, R. Making BaZrS$_3$ Chalcogenide Perovskite Thin Films by Molecular Beam Epitaxy. *Adv. Funct. Mater.* **2021**, *31*, No. 2105563.

(34) Surendran, M.; Chen, H.; Zhao, B.; Thind, A. S.; Singh, S.; Orvis, T.; Zhao, H.; Han, J.-K.; Htoon, H.; Kawasaki, M.; Mishra, R.; Ravichandran, J. Epitaxial Thin Films of a Chalcogenide Perovskite. *Chem. Mater.* **2021**, *33*, 7457–7464.

(35) Ravi, V. K.; Yu, S. H.; Rajput, P. K.; Nayak, C.; Bhattacharyya, D.; Chung, D. S.; Nag, A. Colloidal BaZrS$_3$ Chalcogenide Perovskite Nanocrystals for Thin Film Device Fabrication. *Nanoscale* **2021**, *13*, 1616–1623.

(36) Wang, Y.; Sato, N.; Fujino, T. Synthesis of BaZrS$_3$ by Short Time Reaction at Lower Temperatures. *J. Alloys Compd.* **2001**, *327*, 104–112.

(37) Janz, G. J.; Roduner, E.; Coutts, J. W.; Downey, J. R. Raman Studies of Sulfur-Containing Anions in Inorganic Polysulfides. Barium Trisulfide. *Inorg. Chem.* **1976**, *15*, 1751–1754.

(38) Robinson, P. L.; Scott, W. E. The Polysulphides of Barium and Calcium. *J. Chem. Soc.* **1931**, 693–709.

(39) Massalski, T. B.; Okamoto, H. *Binary Alloy Phase Diagrams*; ASM International: Materials Park, Ohio, 1990.

(40) Comparotto, C.; Davydova, A.; Ericson, T.; Riekehr, L.; Moro, M. V.; Kubart, T.; Scragg, J. Chalcogenide Perovskite BaZrS$_3$: Thin Film Growth by Sputtering and Rapid Thermal Processing. *ACS Appl. Energy Mater.* **2020**, *3*, 2762–2770.

(41) Ramanujam, J.; Singh, U. P. Copper Indium Gallium Selenide Based Solar Cells—a Review. *Energy Environ. Sci.* **2017**, *10*, 1306–1319.

(42) Ferdaous, M. T.; Shahahmadi, S. A.; Chelvanathan, P.; Akhtaruzzaman, M.; Alharbi, F. H.; Sopian, K.; Tiong, S. K.; Amin, N. Elucidating the Role of Interfacial MoS2 Layer in Cu$_2$ZnSnS$_4$ Thin Film Solar Cells by Numerical Analysis. *Solar Energy* **2019**, *178*, 162–172.

(43) Mayer, M.; Möller, S.; Rubel, M.; Widdowson, A.; Charisopoulos, S.; Ahlgren, T.; Alves, E.; Apostolopoulos, G.; Barradas, N. P.; Donnelly, S.; Fazinić, S.; Heinola, K.; Kakuee, O.; Khodja, H.; Kimura, A.; Lagoyannis, A.; Li, M.; Markelj, S.; Mudrinic, M.; Petersson, P.; Portnykh, I.; Primetzhofer, D.; Reichart, P.; Ridikas, D.; Silva, T.; Gonzalez de Vicente, S. M.; Wang, Y. Q. Ion Beam Analysis of Fusion Plasma-Facing Materials and Components: Facilities and Research Challenges. *Nucl. Fusion* **2020**, *60*, No. 025001.

(44) Moro, M. V.; Holeňák, R.; Zendejas Medina, L.; Jansson, U.; Primetzhofer, D. Accurate High-Resolution Depth Profiling of Magnetron Sputtered Transition Metal Alloy Films Containing Light Species: A Multi-Method Approach. *Thin Solid Films* **2019**, *686*, No. 137416.

(45) Arstila, K.; Julin, J.; Laitinen, M. I.; Aalto, J.; Konu, T.; Kärkkäinen, S.; Rahkonen, S.; Raunio, M.; Itkonen, J.; Santanen, J.-P.; Tuovinen, T.; Sajavaara, T. Potku—New Analysis Software for Heavy Ion Elastic Recoil Detection Analysis. *Nucl. Instrum. Methods Phys. Res., Sect. B* **2014**, *331*, 34–41.

(46) Degen, T.; Sadki, M.; Bron, E.; König, U.; Nénert, G. The HighScore Suite. *Powder Diffr.* **2014**, *29*, S13–S18.

(47) Ström, P.; Petersson, P.; Rubel, M.; Possnert, G. A Combined Segmented Anode Gas Ionization Chamber and Time-of-Flight Detector for Heavy Ion Elastic Recoil Detection Analysis. *Rev. Sci. Instrum.* **2016**, *87*, No. 103303.